Simulation of micromechanical behavior of polycrystals: Finite elements vs. fast Fourier transforms

A. Prakash[a,‡] **and R.A. Lebensohn**[b]

[a]Fraunhofer Institut für Werkstoffmechanik, 79108, Freiburg, Germany
[b]Los Alamos National Laboratory, Los Alamos, NM, 87545, USA

E-mail: prakash@iwm.fraunhofer.de, lebenso@lanl.gov

Abstract.

In this work, we compare finite element and fast Fourier transform approaches for the prediction of micromechanical behavior of polycrystals. Both approaches are full-field approaches and use the same visco-plastic single crystal constitutive law. We investigate the texture and the heterogeneity of the inter- and intragranular, stress and strain fields obtained from the two models. Additionally, we also look into their computational performance. Two cases – rolling of aluminium and wire drawing of tungsten – are used to evaluate the predictions of the two models. Results from both the models are similar, when large grain distortions do not occur in the polycrystal. The finite element simulations were found to be highly computationally intensive, in comparison to the fast Fourier transform simulations.

Keywords: Full-field simulations, FFT, FEM, crystal plasticity, fast algorithms, polycrystal simulations, texture

Submitted to: *Modelling Simulation Mater. Sci. Eng.*

1. Introduction

Most materials, manmade or natural, are polycrystals and often exhibit significant elastic/plastic anisotropy that can be ascribed to the behavior of the constituent single crystals. Modeling the micromechanical behavior of these materials, with emphasis on the evolving texture and microstructure, is an active field of research in computational materials science. Optimization of material properties and processes, vis-à-vis development of new materials and products, depends largely on the ability to control and manipulate the evolving anisotropy. Early industrial practice deemed texture to be an inevitable side effect of the manufacturing process. Modern processes, by contrast, aim at optimizing the material properties by exploiting several microstructural mechanisms, such as slip activity, twinning, recrystallization, phase

‡ Corresponding author

transformation etc. Such optimization necessitates robust modeling and simulation tools. Recent advances in theories that link microstructure with macroscopic properties, and development of multi-scale methods have been quite helpful in this regard. The onus is now on efficient algorithmic implementations to complement the developments on the theoretical front, thereby enabling faster, and yet, reliable simulation techniques.

The existing simulation techniques for the prediction of micromechanical behavior of polycrystals can be broadly classified into two categories - mean-field and full-field simulations. The mean-field simulations typically employ homogenization schemes such as Taylor [1938], Sachs [1928], self-consistent models (e.g. Molinari et al. [1987], Lebensohn & Tomé [1993]) etc. Variants of these models – for instance, Taylor-type schemes (e.g. Van Houtte et al. [2004]) and intermediate models (Ahzi & M'Guil [2008]) – primarily aimed at improving texture prediction, have also been proposed. Most of these models, however, overestimate the texture (Kocks et al. [1998], Schmidt et al. [2007]), and hence, the evolving anisotropy. Furthermore, they require significant enhancements, like the n-site implementation (Ahzi [1987], Canova et al. [1992], Solas & Tomé [2001]), or a second-order extension (Ponte Castañeda [2002], Liu & Ponte Castañeda [2004], Lebensohn et al. [2007]) for a realistic prediction of the intra-granular heterogeneity of the stress and strain fields.

Increased computing power in recent years has made full-field simulations a reality, thus providing a more accurate description of the micromechanical fields that develop in the polycrystal. Crystal plasticity FEM with intra-crystalline resolution has been extensively used for this purpose, both with regular (e.g. Becker [1991], Mika & Dawson [1999]) and Voronoi tessellated microstructures (Barbe et al. [2001], Diard et al. [2005]), as also with EBSD based experimental data as input for simulations (e.g. Raabe et al. [2001], Bhattacharyya et al. [2001]). The realistic description of the micromechanical stress and strain fields helps understand the deformation behavior of complex and low symmetry polycrystalline materials like magnesium (Prakash et al. [2009]). However, the difficulty in meshing, coupled with the large number of degrees of freedom required by such calculations, limit the complexity of the problem investigated to representative volume element (RVE) simulations with a few hundred grains.

Recently, a full-field method based on fast Fourier transforms has been proposed as an alternative to small scale FEM. Originally developed as a fast algorithm to compute the elastic and inelastic, effective and local responses of composites (Moulinec & Suquet [1998], Michel et al. [1999]), the FFT algorithm has recently been adapted for polycrystals (Lebensohn [2001]) and successfully used for the prediction of micromechanical behavior of copper (Lebensohn et al. [2008]) and ice (Lebensohn et al. [2009]). As a mesh-free method, the FFT algorithm circumvents the problems that arise due to meshing in FEM simulations.

In this work, we compare the predictive capabilities of both FFT and meso-scale FE solution techniques. The aim is to verify, not only the macroscopic response, but also the micromechanical fields and texture predicted by the two models. Additionally, we

also look into the computation times of the two solution schemes. The plan of the paper is as follows. In section 2 we first present the constitutive model used. Subsequently, in section 3, we discuss the two solution techniques under consideration. The details of the simulations are described in section 4. Results are presented in section 5 and a final discussion is presented in section 6.

2. Constitutive model

The overall behavior of the polycrystal is governed by the individual behavior of its constituents. The polycrystal is assumed to be a periodic structure containing a sufficient number of individual crystals to be representative of the macroscopic behavior of the material under consideration. Each crystal, characterized by a unique initial orientation in the polycrystal, is discretized fine enough to capture the local field behavior.

Imposing an average velocity gradient $\nabla \boldsymbol{V}$ on the periodic microstructure, leads to an average strain rate

$$\dot{\boldsymbol{E}} = \frac{1}{2}\left(\nabla \boldsymbol{V} + \nabla \boldsymbol{V}^T\right), \tag{1}$$

and an average rotation rate

$$\dot{\boldsymbol{\Omega}} = \frac{1}{2}\left(\nabla \boldsymbol{V} - \nabla \boldsymbol{V}^T\right). \tag{2}$$

We now consider the polycrystal at the local level, where all heterogeneities can be distinguished. The local stress and strain rate fields conform themselves to the periodic arrangement of the polycrystal. Let $\boldsymbol{x}$ denote the position of a point in the unit cell and $\boldsymbol{v}(\boldsymbol{x})$, the local velocity field associated with point $\boldsymbol{x}$; then the local strain rate field, which is a function of the local velocity field, can be split into the overall strain rate $\dot{\boldsymbol{E}}$, which would be the actual strain rate field in the unit cell if it were homogeneous, and a fluctuation term $\tilde{\dot{\boldsymbol{\epsilon}}}(\boldsymbol{x})$. The fluctuation term follows from a velocity fluctuation field $\tilde{\boldsymbol{v}}(\boldsymbol{x})$ which accounts for the presence of heterogeneities. The velocity and strain rate fields in the unit cell admit the following decomposition:

$$\begin{aligned} \boldsymbol{v}(\boldsymbol{x}) &= \dot{\boldsymbol{E}} \cdot \boldsymbol{x} + \tilde{\boldsymbol{v}}(\boldsymbol{x}) \\ \dot{\boldsymbol{\epsilon}}(\boldsymbol{v}(\boldsymbol{x})) &= \dot{\boldsymbol{E}} + \tilde{\dot{\boldsymbol{\epsilon}}}(\tilde{\boldsymbol{v}}(\boldsymbol{x})) \qquad \text{with } \tilde{\boldsymbol{v}}(\boldsymbol{x}) \text{ periodic.} \end{aligned} \tag{3}$$

Note that the periodicity of $\tilde{\boldsymbol{v}}$ implies that the average of $\tilde{\dot{\boldsymbol{\epsilon}}}$ in the unit cell vanishes leading to

$$\left\langle \tilde{\dot{\boldsymbol{\epsilon}}} \right\rangle = 0 \quad \Rightarrow \quad \langle \dot{\boldsymbol{\epsilon}} \rangle = \dot{\boldsymbol{E}}, \tag{4}$$

where $\langle \cdot \rangle$ denotes the volumetric average of a quantity over the unit cell of volume V,

$$\langle f \rangle = \frac{1}{|V|} \int_V f(\boldsymbol{x})\, d\boldsymbol{x}. \tag{5}$$

It simply follows that to satisfy equilibrium in the unit cell and between contiguous unit cells, the traction vector has to be anti-periodic. The equilibrium conditions for the local stress $\boldsymbol{\sigma}$ thus read

$$\operatorname{div}(\boldsymbol{\sigma}) = 0; \qquad \boldsymbol{\sigma} \cdot \boldsymbol{n} \text{ antiperiodic}; \tag{6}$$

where $\boldsymbol{n}$ is normal to the unit cell boundary. The overall stress tensor, which in effect is the macroscopic response of the microstructure, is the volume average of the local stresses

$$\boldsymbol{\Sigma} = \langle \boldsymbol{\sigma} \rangle . \tag{7}$$

The local plastic strain rate is given by the sum of the contributions of the crystallographic shear rates (Asaro[1983*a*, 1983*b*])

$$\dot{\boldsymbol{\epsilon}}^p(\boldsymbol{x}) = \sum_{\alpha=1}^{N_s} \boldsymbol{m}^\alpha(\boldsymbol{x}) \dot{\gamma}^\alpha(\boldsymbol{x}), \tag{8}$$

where N_s is the number of active slip systems. The tensor $\boldsymbol{m}^\alpha$ denotes the symmetric Schmid tensor of the system α under consideration, and is defined as

$$\boldsymbol{m}^\alpha = \frac{1}{2} \left(\boldsymbol{s}^\alpha \otimes \boldsymbol{n}^\alpha + \boldsymbol{n}^\alpha \otimes \boldsymbol{s}^\alpha \right), \tag{9}$$

where $\boldsymbol{s}^\alpha$ and $\boldsymbol{n}^\alpha$ are the slip direction and slip plane normal, respectively. The crystalline slip is assumed to obey the rate-sensitivity approximation of the Schmid law, i.e. the slipping rate $\dot{\gamma}^\alpha$ on any particular system α is assumed to depend on the so-called Schmid stress,

$$\dot{\gamma}^\alpha = \dot{\gamma}_0 \left(\frac{\tau^\alpha}{g^\alpha} \right)^n = \dot{\gamma}_0 \left(\frac{\boldsymbol{m}^\alpha : \boldsymbol{\sigma}'}{g^\alpha} \right)^n , \tag{10}$$

where $\dot{\gamma}_0$ is a reference shear rate, $\boldsymbol{\sigma}'$ is the deviatoric stress tensor and τ^α is the resolved shear stress on the system α. The current strength of the slip system g^α is determined by an extended Voce type hardening rule

$$\dot{g}^\alpha = \frac{d\bar{g}^\alpha}{d\Gamma} \sum_\beta h^{\alpha\beta} \dot{\gamma}^\beta, \tag{11}$$

with the hardening function

$$\bar{g}^\alpha = \tau_0 + (\tau_1 + \theta_1 \Gamma) \left[1 - \exp\left(-\frac{\theta_0 \Gamma}{\tau_1} \right) \right], \tag{12}$$

where $h^{\alpha\beta}$ is a hardening matrix whose diagonal elements denote self hardening and off-diagonal elements denote latent hardening. The cumulative shear Γ in the grain is defined as

$$\Gamma = \int_0^t \sum_\alpha \dot{\gamma}^\alpha \, dt. \tag{13}$$

Using eq. (10) in eq. (8), we obtain

$$\dot{\boldsymbol{\epsilon}}^p(\boldsymbol{x}) = \dot{\gamma}_0 \sum_{\alpha=1}^{N_s} \boldsymbol{m}^\alpha(\boldsymbol{x}) \left(\frac{|\boldsymbol{m}^\alpha(\boldsymbol{x}) : \boldsymbol{\sigma}'(\boldsymbol{x})|}{g^\alpha(\boldsymbol{x})} \right)^n \operatorname{sign}\left(\boldsymbol{m}^\alpha(\boldsymbol{x}) : \boldsymbol{\sigma}'(\boldsymbol{x}) \right). \tag{14}$$

It is convenient to define here, the local rotation rate for later use;

$$-\dot{\boldsymbol{\omega}}^p(\boldsymbol{x}) = -\sum_{\alpha=1}^{N_s} \boldsymbol{\beta}^\alpha(\boldsymbol{x})\,\dot{\gamma}(\boldsymbol{x}), \tag{15}$$

where $\boldsymbol{\beta}^\alpha = \frac{1}{2}\left(\boldsymbol{s}^\alpha \otimes \boldsymbol{n}^\alpha - \boldsymbol{n}^\alpha \otimes \boldsymbol{s}^\alpha\right)$, is the antisymmetric Schmid tensor.

3. Solution schemes

3.1. FFT solution scheme

The local stress tensor may be written as

$$\boldsymbol{\sigma}(\boldsymbol{x}) = \mathbb{L}^0 : \dot{\boldsymbol{\epsilon}}^p(\boldsymbol{x}) + \boldsymbol{\phi}(\boldsymbol{x}) - p(\boldsymbol{x})\mathbf{1}, \tag{16}$$

with the polarization field $\boldsymbol{\phi}$ given by

$$\boldsymbol{\phi}(\boldsymbol{x}) = \boldsymbol{\sigma}'(\boldsymbol{x}) - \mathbb{L}^0 : \dot{\boldsymbol{\epsilon}}^p(\boldsymbol{x}), \tag{17}$$

where $\mathbb{L}^0$ is the stiffness of the medium if it were homogeneous. The choice of $\mathbb{L}^0$ is rather arbitrary, but the convergence of the method depends on this choice. In this work, we formulate $\mathbb{L}^0$ as

$$\mathbb{L}^0 = \left\langle \mathbb{M}^{-1} \right\rangle, \tag{18}$$

where $\mathbb{M}$ is a fourth order tensor obtained by rewriting eq. (14) as

$$\dot{\boldsymbol{\epsilon}}^p(\boldsymbol{x}) = \mathbb{M}(\boldsymbol{\sigma}') : \boldsymbol{\sigma}'(\boldsymbol{x}). \tag{19}$$

Equation (16) can now be used to build the equilibrium condition $\sigma_{ij,j} = 0$. Assuming a rigid visco-plastic problem, we have $\dot{\boldsymbol{\epsilon}}^p = \frac{1}{2}\left(\boldsymbol{v} + \boldsymbol{v}^T\right)$, leading to (in component notation)

$$\mathbb{L}^0_{ijkl}\, v_{k,lj} + \phi_{ij,j} - p_{,i} = 0, \tag{20}$$

along with the assumed incompressibility condition

$$v_{k,k} = 0. \tag{21}$$

The above equations (20+21) constitute a system of differential equations that can be solved by means of the Green's functions method. Replacing the polarization term by a unitary body force acting at a given point and along a given direction, we obtain

$$\begin{aligned} \mathbb{L}^0_{ijkl} G_{km,lj}(\boldsymbol{x} - \boldsymbol{x}') + \delta_{im}\delta(\boldsymbol{x} - \boldsymbol{x}') - H_{m,i}(\boldsymbol{x} - \boldsymbol{x}') &= 0 \\ G_{km,k}(\boldsymbol{x} - \boldsymbol{x}') &= 0, \end{aligned} \tag{22}$$

where G_{km} and H_m are the periodic Green's functions associated with the velocity and hydrostatic pressure fields respectively. Assuming that the Green's functions are known, we obtain the velocity fluctuations as a convolution integral:

$$\tilde{v}_k(\boldsymbol{x}) = \int_{\mathbb{R}^3} G_{ki,j}(\boldsymbol{x} - \boldsymbol{x}')\,\phi_{ij}(\boldsymbol{x}')\;\, d\boldsymbol{x}'; \tag{23}$$

its gradient is given by,

$$\tilde{v}_{k,l}(\boldsymbol{x}) = \int_{\mathbb{R}^3} G_{ki,lj}(\boldsymbol{x}-\boldsymbol{x}')\,\phi_{ij}(\boldsymbol{x}')\;\; d\boldsymbol{x}'. \tag{24}$$

Using the property of convolution integrals in direct space being simply products in Fourier space, we can write

$$\begin{aligned} \hat{\tilde{v}}_k(\boldsymbol{\xi}) &= \mathrm{i}\xi_j \hat{G}_{ki}(\boldsymbol{\xi})\hat{\phi}_{ij}(\boldsymbol{\xi}) \\ \hat{\tilde{v}}_{k,l}(\boldsymbol{\xi}) &= -\xi_l\xi_j \hat{G}_{ki}(\boldsymbol{\xi})\hat{\phi}_{ij}(\boldsymbol{\xi}), \end{aligned} \tag{25}$$

where $\boldsymbol{\xi}$ is a point of the Fourier space. The '$\hat{}$' indicates a variable in Fourier space.

The evaluation of the Green's functions can be accomplished by transforming the system of equations (22) to Fourier space.

$$\begin{aligned} \xi_l\xi_j \mathbb{L}^0_{ijkl}\hat{G}_{km} - \mathrm{i}\xi_l \hat{H}_m(\boldsymbol{\xi}) &= \delta_{im} \\ \xi_k \hat{G}_{km}(\boldsymbol{\xi}) &= 0. \end{aligned} \tag{26}$$

Defining a 3x3 matrix A' in Fourier space as $A'_{ik} = \xi_l\xi_j\mathbb{L}^0_{ijkl}$ and the 4×4 matrix A'' as

$$A'' = \begin{bmatrix} A'_{11} & A'_{12} & A'_{13} & \xi_1 \\ A'_{21} & A'_{22} & A'_{23} & \xi_2 \\ A'_{31} & A'_{32} & A'_{33} & \xi_3 \\ \xi_1 & \xi_2 & \xi_3 & 0 \end{bmatrix} \tag{27}$$

we obtain [Lebensohn 2001]

$$\begin{aligned} \hat{G}_{ij}(\boldsymbol{\xi}) &= (A''^{-1})_{ij}, \quad (i,j=1..3) \\ -\mathrm{i}\hat{H}_j(\boldsymbol{\xi}) &= (A''^{-1})_{4j}, \quad (j=1..3), \end{aligned} \tag{28}$$

with

$$\hat{\Gamma}_{ijkl}(\boldsymbol{\xi}) = \xi_j\xi_l\hat{G}_{ik}(\boldsymbol{\xi}). \tag{29}$$

The strain-rate deviation field in the Fourier space is then given by

$$\hat{\tilde{d}}_{ij}(\boldsymbol{\xi}) = -\hat{\Gamma}^{\mathrm{sym}}_{ijkl}(\boldsymbol{\xi})\hat{\phi}_{kl}(\boldsymbol{\xi}) \quad \forall \boldsymbol{\xi}\neq 0 \text{ and } \tilde{d}_{ij}(\mathbf{0}) = 0, \tag{30}$$

where $\hat{\Gamma}^{\mathrm{sym}}_{ijkl}$ is the periodic Green's operator in Fourier space, appropriately symmetrized.

Algorithm

The algorithm can be summarized as follows:

a) Assign initial guess values to the strain-rate field [e.g. $\tilde{\dot{\epsilon}}_{ij}(\boldsymbol{x}) = 0 \Rightarrow \dot{\epsilon}_{ij}(\boldsymbol{x}) = \dot{E}_{ij}$] in the regular grid (direct space) and compute the corresponding stress field ${}^0\sigma_{ij}$ from the local constitutive relation eq. (14); wherein the initial values for the Schmid tensor are obtained from the initial orientation of the grain and the initial values for the critical resolved shear stresses g^α are obtained from the extended Voce hardening law eq. (11).

b) Compute an initial guess for the polarization field in the direct space using eq. (17).

c) Transform the polarization field to the Fourier space

$$\hat{\phi}_{ij}(\boldsymbol{\xi}) = \mathcal{F}(\phi_{ij}(\boldsymbol{x})). \tag{31}$$

d) Based on the iterative procedure of augmented Lagrangeans proposed by MICHEL ET AL. [2000], and assuming the initial guess for the Lagrange multipliers as

$${}^{0}\lambda_{ij}(\boldsymbol{x}) = {}^{0}\sigma'_{ij}(\boldsymbol{x}), \tag{32}$$

the new guess (n+1 iteration) for the strain rate is given by eq. (30).

e) The strain-rate deviation in direct space can be obtained by applying the inverse Fourier transform

$${}^{n+1}\tilde{d}_{ij}(\boldsymbol{x}) = \mathcal{F}^{-1}\left\{ {}^{n+1}\hat{\tilde{d}}_{ij}(\boldsymbol{\xi}) \right\}. \tag{33}$$

f) The new guess for the deviatoric stress field can be computed by the following equation:

$$\begin{aligned} {}^{n+1}\boldsymbol{\sigma}'(\boldsymbol{x}) \quad &+ \quad \mathbb{L}^0 : \gamma_0 \sum_{\alpha=1}^{N} \boldsymbol{m}^{\alpha}(\boldsymbol{x}) \left(\frac{\boldsymbol{m}^{\alpha} : {}^{n+1}\boldsymbol{\sigma}'}{g^{\alpha}} \right)^{n} \\ &= \quad {}^{n}\boldsymbol{\lambda}(\boldsymbol{x}) + \mathbb{L}^0 : \left(\dot{E} + {}^{n+1}\tilde{\boldsymbol{d}}(\boldsymbol{x}) \right). \end{aligned} \tag{34}$$

The above 5x5 system of non-linear equations is solved by the Newton-Raphson method.

g) The iteration is complete with the calculation of the new guess of the Lagrange multiplier field.

$${}^{n+1}\boldsymbol{\lambda}(\boldsymbol{x}) = {}^{n}\boldsymbol{\lambda}(\boldsymbol{x}) + \mathbb{L}^0 : \left({}^{n+1}\tilde{\dot{\boldsymbol{\epsilon}}} - {}^{n+1}\tilde{\boldsymbol{d}} \right). \tag{35}$$

Equations (34) and (35) guarantee the convergence of, (i) the strain rate field $\dot{\boldsymbol{\epsilon}}(\boldsymbol{x})$ associated with the constitutive equation with the kinematically admissible strain rate field $\boldsymbol{d}(\boldsymbol{x})$ to fulfill compatibility, and (ii) the Lagrange multiplier field $\boldsymbol{\lambda}(\boldsymbol{x})$ towards the deviatoric stress field $\boldsymbol{\sigma}'(\boldsymbol{x})$, to fulfill equilibrium.

Texture and morphology update

Upon convergence, the local crystallographic lattice rotations are updated with the following relation:

$$\boldsymbol{\omega}(\boldsymbol{x}) = \left[\dot{\boldsymbol{\Omega}}(\boldsymbol{x}) + \tilde{\dot{\boldsymbol{\omega}}}(\boldsymbol{x}) - \dot{\boldsymbol{\omega}}^{p}(\boldsymbol{x}) \right] \Delta \mathrm{t}, \tag{36}$$

where $-\boldsymbol{\omega}^{p}(\boldsymbol{x})$ is given by eq. (15) and $\tilde{\dot{\boldsymbol{\omega}}}(\boldsymbol{x})$ is obtained by using the converged antisymmetric field:

$$\hat{\tilde{\dot{\boldsymbol{\omega}}}}(\boldsymbol{\xi}) = -\hat{\boldsymbol{\Gamma}}^{\mathrm{antisym}}(\boldsymbol{\xi}) : \hat{\boldsymbol{\phi}}(\boldsymbol{\xi}) \tag{37}$$

After each time increment, the new position of the Fourier points can be determined by the following equation

$$\bar{\boldsymbol{x}} = \boldsymbol{x} + \left(\dot{\boldsymbol{E}}\boldsymbol{x} + \tilde{\boldsymbol{v}} \right) \Delta \mathrm{t} \tag{38}$$

where $\tilde{\boldsymbol{v}}$ is obtained from (23). It is evident that the above equation for the morphology update would entail the usage of two grids - a regular Fourier grid and a material-point grid that would allow following the morphology of individual grains. In the present work, however, a simplified morphology update neglecting the velocity fluctuation term is used. Equation (38) thus reduces to

$$\bar{\boldsymbol{x}} = \boldsymbol{x} + \dot{\boldsymbol{E}}\boldsymbol{x}\ \Delta\mathrm{t}, \tag{39}$$

resulting in a regular Fourier grid after each increment. The distances between adjacent points, however, do change. Thus the morphology update of individual grains is determined by an *average stretching* prescribed by the macroscopic deformation. The implications of the approximation involved in this simplified morphology update algorithm are discussed in section 6.

It must be noted that the FFT solution scheme, presented thus far, is completely visco-plastic and ignores elastic stretching.

3.2. FE solution scheme

The basic premise of the finite element method is quite well known and has been extensively used for various purposes. For detailed information on FEM, the reader is referred to standard textbooks on the subject. In this section, we only discuss the implementation of the constitutive model.

The constitutive model described in section 2 has been programmed as a user material (UMAT) subroutine for the finite element package ABAQUS Standard®(Huang [1991], Prakash et al. [2009]). Although the constitutive model is entirely as described before, the implementation is slightly different. In contrast to the current implementation of the FFT algorithm where elastic stretching is ignored, the FE solution scheme treats elastic response as a part of the total material response.

The elastic response $\boldsymbol{F}^*$ of the material is obtained as a result of the multiplicative split of the deformation gradient $\boldsymbol{F}$:

$$\boldsymbol{F}^* = \boldsymbol{F}\boldsymbol{F}^{p-1}, \tag{40}$$

where $\boldsymbol{F}^p$ denotes the plastic shear. The rate of change of $\boldsymbol{F}^p$ is related to the slipping rate $\dot{\gamma}^\alpha$ of the slip system by

$$\dot{\boldsymbol{F}}^p\boldsymbol{F}^{p-1} = \sum_\alpha \dot{\gamma}^{(\alpha)}\boldsymbol{s}^{(\alpha)} \otimes \boldsymbol{n}^{(\alpha)} \tag{41}$$

which is equivalent to eq. (8). The orientation update at a Gauss point is given by the update of slip direction $\boldsymbol{s}^{(\alpha)}$ and slip plane normal $\boldsymbol{n}^{(\alpha)}$

$$\begin{aligned} \boldsymbol{s}^{*(\alpha)} &= \boldsymbol{F}^*\,\boldsymbol{s}^{(\alpha)} \\ \boldsymbol{n}^{*(\alpha)} &= \boldsymbol{n}^{(\alpha)}\boldsymbol{F}^{*-1}. \end{aligned} \tag{42}$$

In addition to the elastic response, morphology update of grains is realized through an updated Lagrangean formulation. This allows for complex grain shapes to be predicted.

4. Simulation aspects

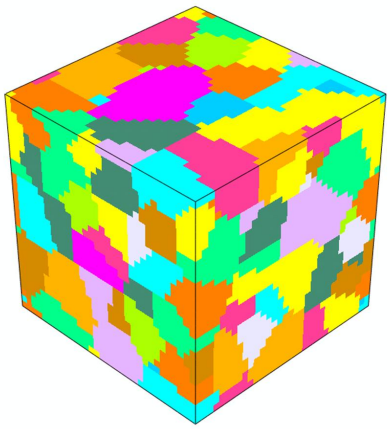

Figure 1: A 100 grain RVE used in the simulations

In order to ascertain the capabilities of the FFT algorithm, a numerical experiment comparing FFT with FE simulations was performed. For this purpose, the results from FE simulation are assumed to be the standard. Since the FFT solution scheme is restricted to periodic media, a unit cell consisting of 100 grains with periodic grain structure is used (figure 1). Additionally, periodic boundary conditions are imposed on the RVE, thereby coupling two points on opposite faces of the RVE with the macroscopic deformation gradient. The unit cell is discretized with a regular grid of 32x32x32 elements (voxels in the case of FFT). Linear brick elements are used in the case of FE, giving an average of 2600 Gauss points per grain.

Case	Slip system	Hardening parameters			
		τ_0	τ_1	θ_0	θ_1
Rolling	$\{111\}\langle 110\rangle$	47.0	86.0	550.0	16.0
Wire Drawing	$\{110\}\langle 111\rangle$	175.33	80.0	40.0	0.0

Table 1: Voce hardening parameters

Two different cases were chosen for the study - a) rolling of aluminium and b) drawing of tungsten wires. A single slip mode was assumed to be active in both cases, i.e. $\{111\}\langle 110\rangle$ in aluminium and $\{110\}\langle 111\rangle$ in tungsten. The Voce hardening parameters used in this study are presented in table 1. The hardening matrix of the Voce hardening law eq. (11) is set to 1.0 for both self and latent hardening. The same set of parameters is used for both FE and FFT simulations. An initial random texture was assumed in the case of rolling of aluminium, while a sharp $\langle 110\rangle$ texture in the drawing direction was used in the case of tungsten. All the simulations employ a constant strain rate of 1.0. Rolling is idealized as plane strain compression, while wire drawing is idealized as

biaxial compression. Post processing of the results is done in Abaqus Viewer®with user scripts written in Python, ensuring consistency in the contour plots obtained.

The exponent in the constitutive relation (14), n, is assumed to be 10.0. Note that the corresponding rate-sensitivity ($m = 1/n = 0.1$) is larger than the typical values for cubic metals at room temperature ($m \approx 0.001$, i.e. $n \approx 1000$). However, the use of exponents of that order would result in numerical instabilities in both methods (maximum values of n for well-behaved simulations are of the order of 50). Therefore, (14) should be regarded as an approximation for better numerical tractability of the rate-insensitive crystal plasticity approach based on the Schmid law, rather than a tool to study quantitatively rate-sensitivity effects.

5. Results

5.1. Macroscopic response

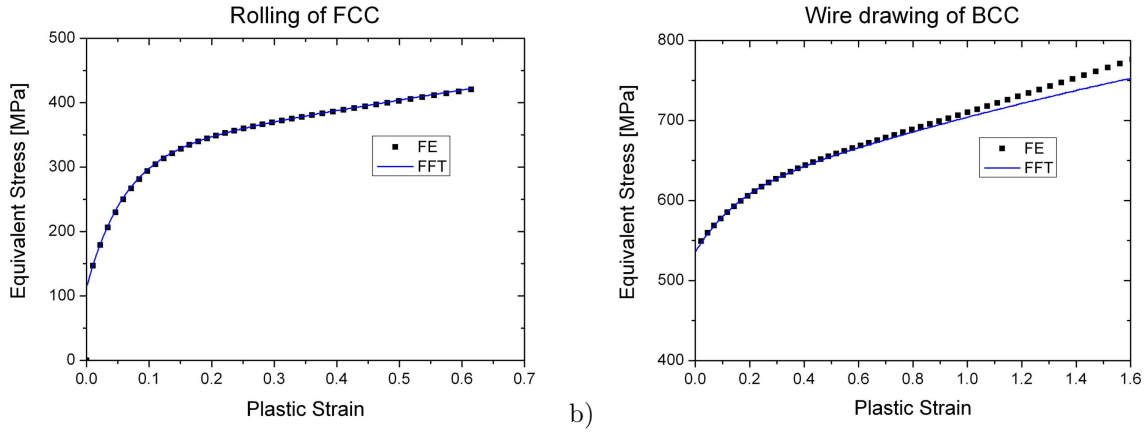

Figure 2: Macroscopic response from the rolling simulations; a) Rolling of aluminium, b) wire drawing of tungsten

Figure 2 shows the stress vs. strain curves obtained from the simulations. In the case of the rolling simulations, the response from FFT is almost identical to that of FE. The curves obtained from the wire drawing simulations also follow similar trends upto a strain of around 0.4. With increasing strain, however, the curves diverge. The primary reason for this deviation is the severe distortion of grains in the polycrystal, leading to the well-known grain curling phenomenon. Further discussion is presented in section 6.

5.2. Local response

5.2.1. Rolling of Aluminium The deformed configuration of the polycrystal after 40% thickness reduction is shown in figure 3. The loading directions are marked as RD - rolling direction, TD - transverse direction and ND - normal direction. In comparison to FE, where one observes a slightly distorted shape of the polycrystal and

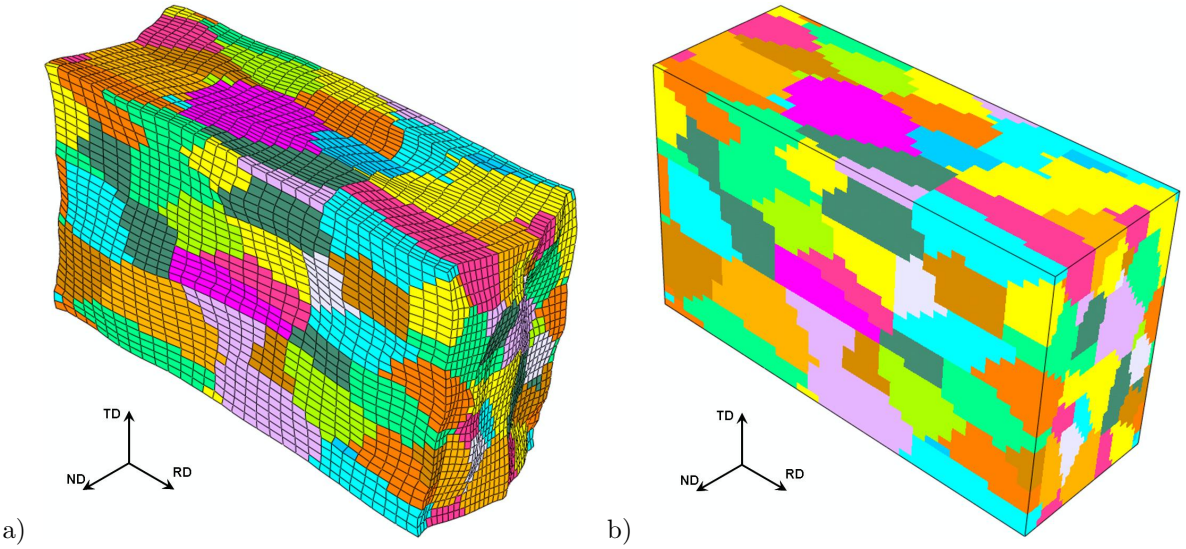

a) b)

Figure 3: Deformed configuration of the RVE from rolling simulations after 40% thickness reduction; a) FE, b) FFT

individual grains, FFT yields a homogeneous shape, which is clearly a result of the approximate shape update algorithm used.

The effect of these slight distortions on the local field response is minimal. The distribution of the accumulated plastic strain and stresses in the RVE can be seen in figure 4. To ensure shape conformity, the results are plotted on the undeformed configuration of the RVE. Localized plastic zones forming regions of high and low plastic strain can be seen in the polycrystal. In the transverse direction, shear bands at approximately 45° to the rolling direction can be observed in both simulations. The stress distribution pattern in the RVE predicted by both models is also similar. It is interesting to note that the location of these localized zones (both stress and strain) are predicted at the same places by both models. The absolute amount of localization does vary, albeit only slightly. Even with a relatively primitive shape update scheme, the results from the FFT algorithm are encouraging and comparable with FE.

5.2.2. Drawing of tungsten wires Tungsten exhibits extreme grain distortions during the wire drawing process leading to the well known grain curling phenomenon (Hosford [1964], Očenášek et al. [2007]). Figure 5a shows the deformed configuration of the RVE from FE simulations, where WA denotes the wire axis. After a diameter reduction of 50%, large distortions in individual grains are observed. Curled grains can be clearly seen when viewed in the cross-section (see inset). Due to the absence of a sophisticated shape update algorithm, the phenomenon of grain curling cannot be described by FFT (the deformed configuration is similar to that seen during rolling and hence is not shown pictorially). This leads to a deviation in the local field distribution in the RVE. At a moderate strain of 10%, however, the distortion of grains in the FE simulation is minimal (figure 5b). Grains experience a stretching in the longitudinal direction, whilst

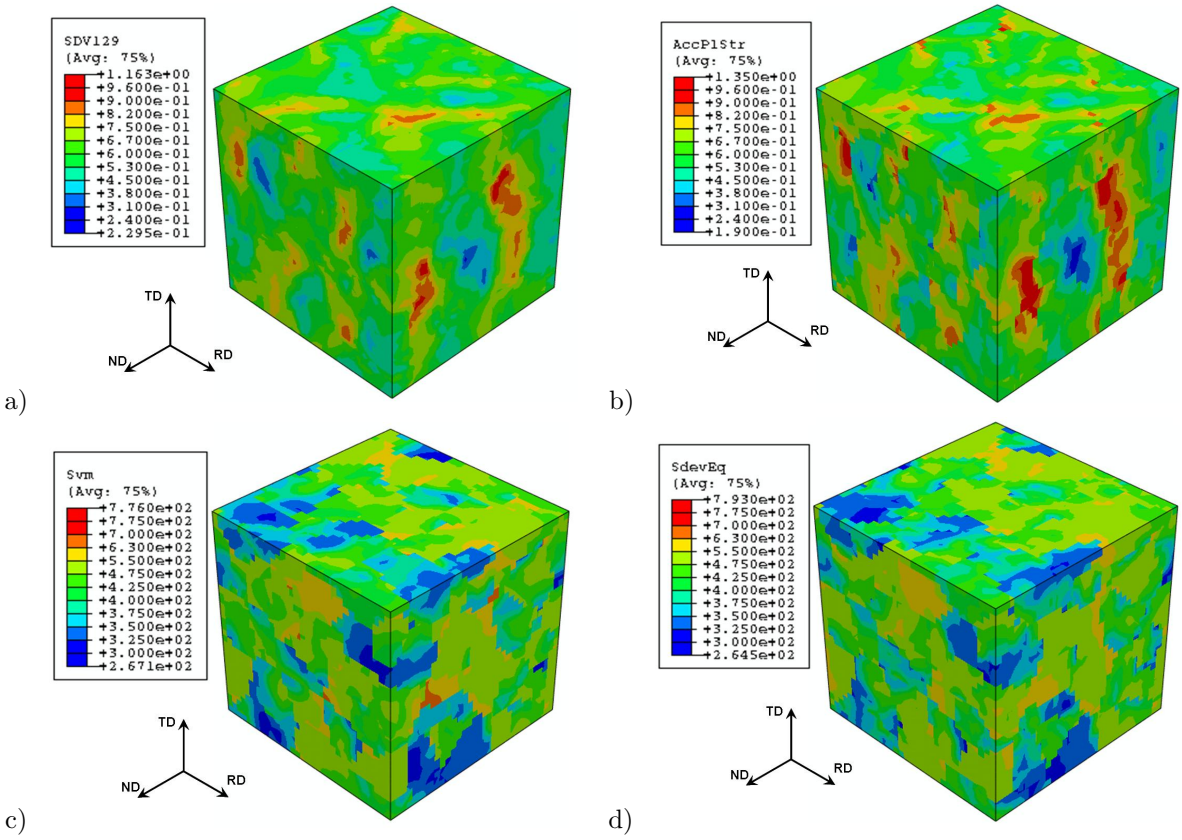

Figure 4: Results from rolling simulations; *top row* - distribution of accumulated plastic strain, *bottom row* - stress distribution; *left* - FE, *right* - FFT. Note that the scales used for comparison are the same; only the maximum and minimum values differ.

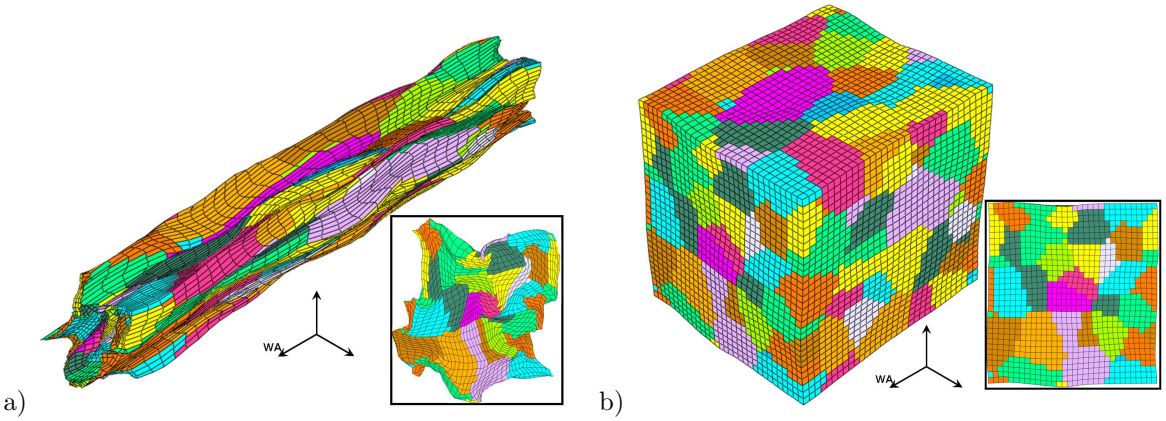

Figure 5: Deformed configuration of the RVE calculated with FE in the wire drawing case - a) after 50% diameter reduction, b) after 10% equivalent strain (Inset - cross sectional views)

undergoing little change in shape in the cross-section. The field distribution at this moderate strain is quite comparable (figure 6). As in the case of the rolling simulations, the pattern of stress and strain distribution is similar; the absolute values of the field quantity, especially at grain boundaries, differ slightly.

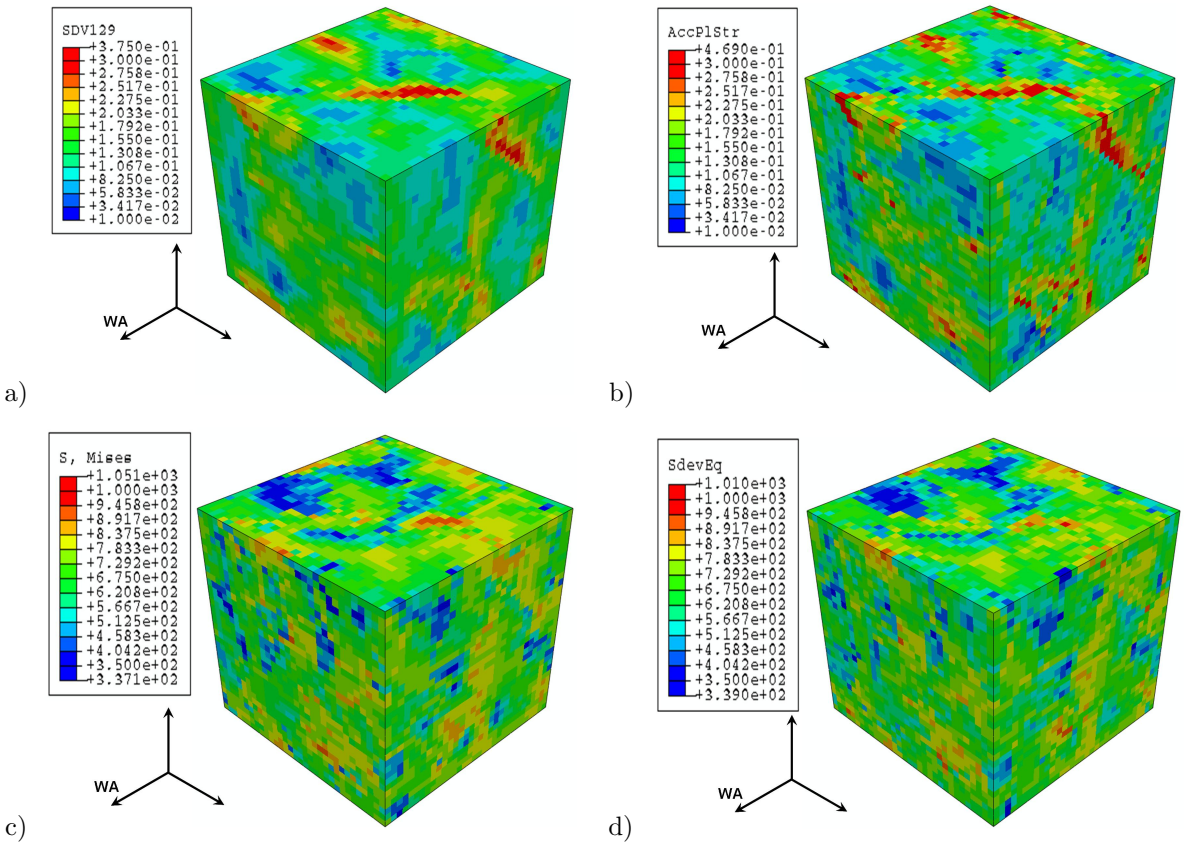

Figure 6: Results from wire drawing simulations at 10% equivalent strain; *top row* - distribution of accumulated plastic strain, *bottom row* - stress distribution; *left* - FE, *right* - FFT. Note that the scales used for comparison are the same; only the maximum and minimum values differ.

5.3. Texture results

The texture results from the simulations are presented in figures 7 and 8. Almost identical results are obtained in both the rolling and wire drawing simulations. We recall that an initial random texture was used for the rolling simulations, while a $\langle 110 \rangle$ texture in the drawing direction was used for the wire drawing simulation. As evident from the figures, the texture predicted by both models is almost identical and conforms to the ideal rolling texture of *fcc* materials [Kocks et al. 1998]. In the case of the wire drawing simulations, a sharp $\langle 110 \rangle$ texture is obtained in the wire axis, which is also along expected lines.

It is worth noting that these textures obtained with models like FE and FFT, that consider the heterogeneity of the mechanical fields inside the grains (in particular

the lattice rotation field), are in general, of lesser intensity than similar simulations involving a lower level of fidelity (i.e. based on the sole determination of the average values of the mechanical fields in the grains), like the Taylor or the 1-site viscoplastic self-consistent (VPSC) model (Lebensohn & Tomé [1993]), and in better agreement with experimental textures. Such improved agreement has been already reported by, e.g. Dawson & Beaudoin [1998] in the case of FE and by and Lebensohn [2001] in the case of FFT.

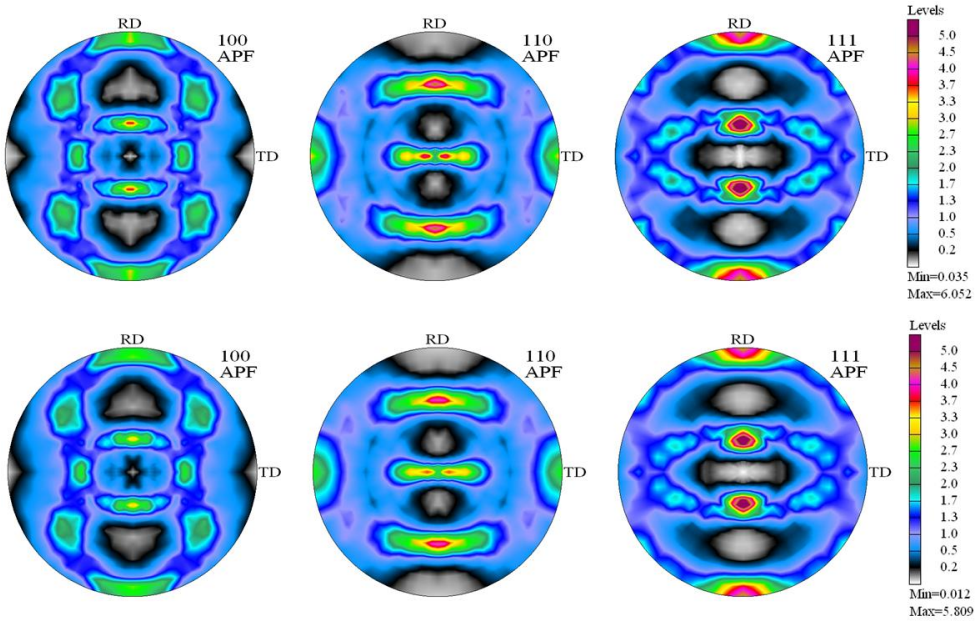

Figure 7: Texture results from rolling simulations after 40% thickness reduction; *Top row* - FE, *Bottom row* - FFT

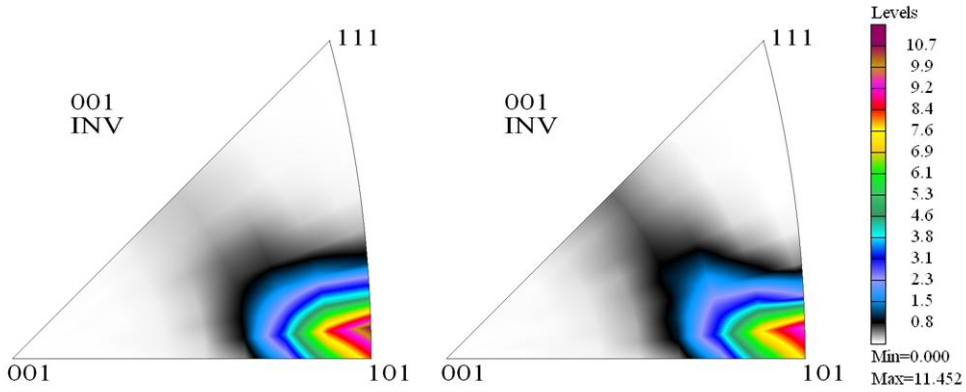

Figure 8: Inverse pole figures of the wire axis obtained from wire drawing simulations; *left* - FE, *right* - FFT

5.4. Computation times

All computations presented in this work were run on an Intel®Xeon®2.6GHz machine with 8 *cpu*s and 16GB shared memory. While the FE computations were multiple *cpu* runs with 4 *cpu*s, all FFT computations were single *cpu* runs. The computation times are shown in figure 9, along with the actual values also tabulated. No correction has been made for FE simulations with multiple *cpu*s. For the same discretization of 32^3 elements, the FFT computation times were in the order of hours, while the FE computations took over 5 days. With an increased resolution of 64^3 voxels, the computation times with FFT also increase, but they are still lower than those corresponding to the multiple *cpu* FE simulations with 32^3 elements.

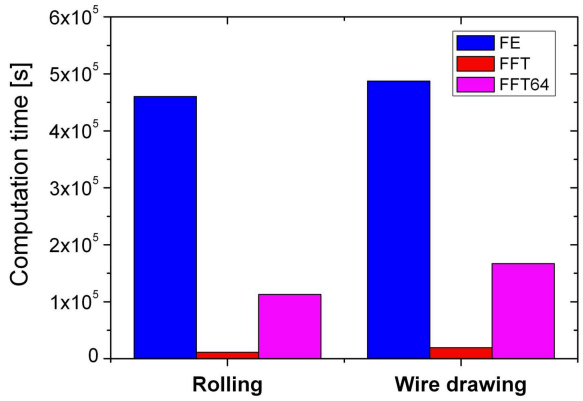

	Rolling	Wire Drawing
FE	4.60e5 *s*	4.87e5 *s*
FFT	1.12e4 *s*	1.94e4 *s*
FFT64	1.13e5 *s*	1.67e5 *s*

Figure 9: Comparison of computation times from FE (32^3 elements), FFT (32^3 voxels) and FFT64 (64^3 voxels) simulations

6. Discussion

A numerical experiment comparing two full-field simulations (for the prediction of micromechanical behavior of polycrystals) has been performed in this work. In particular, a new method based on fast Fourier transforms is compared with the conventional FE method; not only for the predictive capability, but also computational efficiency. Both computation schemes use the same constitutive model, the details of which have been presented in section 2. In the case of the finite element method, the equilibrium equations are solved piecewise by discretizing the structure with finite elements to obtain a equation of the form $\boldsymbol{K} \cdot \boldsymbol{U} = \boldsymbol{P}$, where $\boldsymbol{K}$ is the stiffness matrix, $\boldsymbol{U}$ is the displacement vector and $\boldsymbol{P}$ is the load vector. By contrast, the FFT method uses Green's functions to reformulate the equilibrium conditions, with the solution of the unknown variables described as convolution integrals. These convolution integrals are then transformed to the Fourier space and the values of the actual unknowns in direct space are obtained by transforming the solutions back from the Fourier space.

In this work, both methods were used to simulate two test cases - a) rolling of FCC and b) drawing of BCC wires. The results from the simulations are very encouraging.

The deformation characteristics predicted by both models are qualitatively similar, with both models predicting large plastic deformation in almost the same regions of the RVE. Additionally, localized shear zones at approximately 45° could be observed in the rolling simulations when viewed in the transverse direction. The same trends could also be observed in the wire drawing simulations at 10% strain.

Due to lack of a sophisticated computation scheme for the shape update of grains, a quantitative comparison of the stress and strain fields was not possible. In the case of the rolling simulations, the simple shape update algorithm in FFT does not act as a major drawback for the prediction of the local fields in the polycrystal, as the grains more-or-less follow an average stretching prescribed by the macroscopic deformation. However, in the case of the wire drawing simulations, a more complex morphology update algorithm is necessary. After 50% diameter reduction, large distortions of grains are observed. This not only leads to a deviation in the macroscopic stress vs. strain response, but also gives rise to huge variations in the local field response. At a much lower strain of 10%, where the distortion of grains is not too high, the local fields predicted by FFT are consistent with the results from FE. A more sophisticated shape update of grains based on for instance, the particle-in-cell (PIC) method (Sulsky et al. [1995], Lahellec et al. [2001]) is necessary for simulations where grain distortions play a major role.

An additional point of comparison was the computational efficiency of both models. For a complete one-on-one comparison, an improved shape update algorithm is necessary. Nevertheless, for the rolling simulations for *fcc* materials, where the current implementation suffices, the computation times with FFT are much lower than FE. A major part of the computation time in FE is invested in the time-consuming inversion of the stiffness matrix of the global solution equation. By contrast, the FFT-based approach requires the repetitive inversion of a 4×4 matrix (see equation 27) and application of the very efficient FFT algorithm. This clearly indicates that FFT is a computationally efficient alternative to the conventional FE-based approach to simulate the micromechanical behavior of periodic microstructures.

7. Conclusions

Crystal plasticity FEM is a well-established numerical tool to predict texture and microstructure evolution of polycrystals with intra-crystalline resolution and general boundary conditions. Alternative FFT-based methods have been proposed in recent years for the same purpose, albeit restricted to periodic boundary conditions. The FFT-based framework shows a great potential, especially because of its high numerical efficiency. The original contribution of the present work is to have demonstrated a fairly good agreement between the predictions of the novel FFT and the standard FEM. In particular, we have shown that:

a) The FFT algorithm is an efficient alternative solution scheme to the more commonly used small-scale FEM for the prediction of micromechanical behavior

of polycrystals. For the same geometry and resolution, computation times of FE simulations far exceed those of FFT.

b) Stress and strain distribution patterns predicted by FFT are similar and comparable to those of FE.

c) The macroscopic response from rolling simulations is almost identical. In the wire drawing simulations, the FFT response deviates slightly from the FE response at large strains; the main reason being the approximation in the shape update algorithm used in FFT.

d) Texture results from both solution schemes are also almost identical. Starting from an initial random texture, a typical rolling texture is obtained in the case of rolling simulations, while the initial $\langle 110 \rangle$ texture in the wire axis is maintained in the wire drawing simulations.

e) A more sophisticated shape update algorithm is required in FFT for the prediction of realistic morphology evolution like the grain curling phenomenon in *bcc* wires. The present shape update suffices for cases where grains do not deviate significantly from the average stretching prescribed by the macroscopic deformation gradient.

f) Evidently, the simplifications used in the FFT formulation have a significant contribution in speeding-up the calculation; whilst the consideration, in FEM, of elasticity, geometric nonlinearity, more accurate grain morphology update, etc. appear to be not relevant to the output of interest in the present simulations – i.e. texture evolution, local mechanical fields and effective behavior, except when the grain morphology becomes extremely distorted, like in the case of wire drawing of *bcc* materials.

Acknowledgments

AP acknowledges the partial support of the German research foundation (DFG) under the framework of the priority program SPP1168 (Grant no. Ri 329). The discussions with Prof. Hermann Riedel and Dr. Ingo Schmidt are also acknowledged. The authors also thank the support of Dr. Alexander Butz in the generation of RVEs.

References

Ahzi S 1987 A Self-consistent Approach to the Behaviour of Viscoplastic Polycrystals during Large Deformations PhD thesis Université de Metz.

Ahzi S & M'Guil S 2008 *Acta Materialia* **56**, 5359–5369.

Asaro R J 1983*a* *Journal of Applied Mechanics* **50**, 921–934.

Asaro R J 1983*b* *Advances in Applied Mechanics* **23**, 1–115.

Barbe F, Decker L, Jeulin D & Cailletaud G 2001 *International Journal of Plasticity* **17**, 513–536.

Becker R 1991 *Acta Metallurgica et Materialia* **39, No 6**, 1211–1230.

Bhattacharyya A, El-Danaf E, Kalidindi S & Doherty R 2001 *International Journal of Plasticity* **17**, 861–883.

Canova G, Wenk H & Molinari A 1992 *Acta Materialia* **40**, 1519–1530.

Dawson P R & Beaudoin A J 1998 *in* 'Texture and Anisotropy' Cambridge University Press pp. 512–531.
Diard O, Leclercq S, Rousselier G & Cailletaud G 2005 *International Journal of Plasticity* **21**, 691–722.
Hosford W 1964 *Transactions of the AIME* **230**, 12–15.
Huang Y 1991 A user-material subroutine incorporating single crystal plasticity in the abaqus finite element program Technical Report MECH-178 Harvard University.
Kocks U F, Tomé C N & Wenk H R 1998 *Texture and Anisotropy* 1 edn Cambridge University Press.
Lahellec N, Michel J C, Moulinec H & Suquet P 2001 *in* C Miehe, ed., 'IUTAM Symposium on computational mechanics of solids materials.' Dordretch, Kluwer Academic pp. 247–258.
Lebensohn R A 2001 *Acta Materialia* **49**, 2723–2737.
Lebensohn R A, Brenner R, Castelnau O & Rollett A D 2008 *Acta Materialia* **56(15)**, 3914–3926.
Lebensohn R A, Montagnat M, Mansuy P, Duval P, Meysonnier J & Philip A 2009 *Acta Materialia* **57**, 1405–1415.
Lebensohn R A & Tomé C N 1993 *Acta Metallurgica et Materialia* **41, No. 9**, 2611–2624.
Lebensohn R A, Tomé C N & Ponte Castañeda P 2007 *Philosophical Magazine* **87**, 4287–4322.
Liu Y & Ponte Castañeda P 2004 *Journal of the Mechanics and Physics of Solids* **52**, 467–495.
Michel J, Moulinec H & Suquet P 1999 *Computer Methods in Applied Mechanics and Engineering* **172**, 109–143.
Michel J, Moulinec H & Suquet P 2000 *Computer Modeling in Engineering and Sciences* **1(2)**, 79–88.
Mika D & Dawson P 1999 *Acta Materialia* **47 (4)**, 1355–1369.
Molinari A, Canova G & Ahzi S 1987 *Acta Metallurgica* **35**, 2983–2994.
Moulinec H & Suquet P 1998 *Computer Methods in Applied Mechanics and Engineering* **157**, 69–94.
Očenášek J, Rodriguez-Ripoll M, Weygand S M & Riedel H 2007 *Computational Materials Science* **39**, 23–28.
Ponte Castañeda P 2002 *Journal of the Mechanics and Physics of Solids* **50**, 737–757.
Prakash A, Weygand S M & Riedel H 2009 *Computational Materials Science* **45**, 744–750.
Raabe D, Sachtleber M, Zhao Z, Roters F & Zaefferer S 2001 *Acta Materialia* **49**, 3433–3441.
Sachs G 1928 *Zeitschrift des Vereines Deutscher Ingenieure* **72**, 734–736.
Schmidt C, Kawalla R, Walde T, Riedel H & Prakash A 2007 *Proceedings of Thermec 2006, Vancouver, Materials Science Forum* **539-543**, 3448–3453.
Solas D E & Tomé C N 2001 *International Journal of Plasticity* **17**, 737–753.
Sulsky D, Zhou S J & Schreyer H L 1995 *Computer Physics Communications* **87**, 236–252.
Taylor G I 1938 *Journal of the Institute of Metals* **62**, 307–327.
Van Houtte P, Li S & Engler O 2004 *in* D Raabe, F Roters, F Barlat & L.-Q Chen, eds, 'Continuum Scale Simulation of Engineering Materials' pp. 459–472.